Modeling and design of a semi-continuous fluidized bed pellet reactor

Lie-Ding Shiau[a,b], Hsuan-Yu Wu[c], Jeffrey D. Ward[c,*]

[a]Department of Chemical and Materials Engineering, Chang Gung University, Taoyuan, Taiwan, email: shiau@mail.cgu.edu.tw
[b]Department of Urology, Chang Gung Memorial Hospital, Linkou, Taiwan
[c]Department of Chemical Engineering, National Taiwan University, Taipei 106-07, Taiwan, emails: jeffward@ntu.edu.tw (J.D. Ward), r03524070@ntu.edu.tw (H.-Y. Wu)

ABSTRACT

A mathematical model is developed in this paper to describe the operation of fluidized bed pellet reactor (FBPR) operating semi-continuously with liquid recycle. The reactor is designed to remove targeted ions from wastewater by reaction to form a sparingly soluble salt which precipitates on the seed pellets. The model can determine the variations of the ion concentration, the pellet size, and the voidage along the bed height during operation. In addition, it also allows one to calculate the effect of the reagent concentration and the recirculation ratio on the effluent ion concentration. A design procedure for FBPRs based on the model is also proposed.

Keywords: Flow behavior; Modeling; Fluidized bed; Pellet reactor; Precipitation

1. Introduction

In recent years, fluidized bed pellet reactors (FBPRs) have been extensively applied in three areas including: (1) the softening of drinking and process water [1–7], (2) the removal of phosphates from industrial and municipal wastewater [8–21], (3) removal of fluoride [22–28], and (4) the removal and recovery of heavy metals and anions [29–43]. In the traditional unseeded precipitation treatment of wastewater where a dissolved component has to be removed, the addition of precipitating chemicals results in the formation of sludge. Then the sludge produced must be transported to and disposed of in a waste landfill. On the contrary, a major advantage of the FBPRs is the production of a small amount of water-free, reusable pellets, without extra surplus sludge production. For instance, the $CaCO_3$ pellets produced in water softening can be sold to the livestock feed industry; the $Ca_3(PO_4)_2$ pellets produced in phosphate removal can be sold to the phosphate processing industry; the $NiCO_3$ pellets produced in nickel recovery can be dissolved in a strong acid to recover a pure concentrated metal solution, which can be reused in the metal-finishing, the metal processing or the chemical industry. Another characteristic of the FBPRs is that the fluidization of pellets provides a large crystallization surface, so that the process operates at high rate and with high efficiency. Consequently, the system is compact, requires a relatively low investment, and has low operational costs.

Recirculation is commonly applied in FBPRs [43]. Recirculation provides a number of benefits including damping fluctuations in flow and contaminant concentration in the wastewater, increasing operational flexibility, diluting the feed to prevent primary nucleation in the reactor and ensuring that the bed remains fluidized at all times.

Due to the increasing application of FBPRs, a number of studies on the performance of FBPRs have been reported [44–54]. These studies mainly concentrated on the experimental investigation of the process conditions on the performance of FBPRs. In this paper, a mathematical model will be presented to simulate the flow behavior of FBPRs. The effect of process conditions, such as influent reagent concentration and circulation ratio on the performance of an FBPR will be investigated in the example calculations.

* Corresponding author.

The simulation results can provide useful guide to optimize the operation parameters in the design of an FBPR.

2. Mathematical model

A schematic diagram of a typical FBPR is shown in Fig. 1. An aqueous stream is pumped in an upward direction through a cylindrical pellet reactor containing about 10% (wt%) seeds, such as filter sands, and the pellet bed is kept in the fluidized state. The supersaturation for crystallization is maintained by the dosage of a suitable chemical. As the mixture of recirculation and influent streams is injected at the bottom of the reactor, supersaturation is at a maximum at the bottom and approaches zero at the top of the fluidized bed. Supersaturation is kept within the metastable region to avoid nucleation along the reactor. As a consequence, the pellets near the bottom grow faster in size and weigh more than those near the top of the reactor. Periodically, pellets are washed from the bottom of the reactor and fresh pellets are added, while clean water leaves via an overflow at the top of the reactor. The flow behavior in the above-mentioned FBPRs is quite complex since it is an unsteady state operation and the ionic concentration, the pellet size and the voidage along the bed height vary during the operation.

Shiau et al. [55] developed a mathematical model to simulate the flow behavior of crystal growth in a fluidized bed crystallizer operated in a batch mode. In the operation of the fluidized bed crystallization, supersaturation is generated by cooling a concentrated solution to a temperature below the solute solubility temperature. Seed crystals are initially placed in the crystallizer and allowed to grow as the supersaturated solution is pumped continuously into the bottom of the crystallizer. On the other hand, in the FBPRs described in this work, supersaturation is created by mixing the contaminated wastewater with the reagent solution. The seeds, such as filter sands, are initially placed and kept in the fluidized state. Then solid product precipitates onto the surface of the seeds during the operation. In addition, recirculation is generally employed in an FBPR while there is no recirculation present in the crystallization model developed by Shiau et al [55]. In view of the differences of the flow behavior between a fluidized bed crystallizer and an FBPR, a mathematical model will be developed in this section to simulate the FBPR operation. In the development of the model, the following assumptions are made:

(1) the seeds are initially uniform-sized,
(2) the seeds are spherical and remain spherical during the growth,
(3) no breakage of pellets occurs,
(4) the supersaturation is kept within the metastable region so that spontaneous precipitation will not form,
(5) the liquid phase moves upward through the bed in plug flow,
(6) the fluidized bed is perfectly mixed in the radial direction and perfectly segregated in the axial direction (analogous to the assumptions in a plug flow reactor).

To simulate the precipitation process of an FBPR described above, the fluidized bed is subdivided into N stages each of which contains pellets of equal size and solutions of equal supersaturation as depicted in Fig. 2. As N approaches infinity, assumptions (5) and (6) will be satisfied. Each stage contains the same number of pellets. As the operation proceeds, the height of each stage will change with time as the fluid flow rate changes and the particles grow. We consider that an influent containing A^{+x} ion mixes with the chemical reagent containing B^{-y} ion to form A_aB_b precipitation on the pellet surface:

$$aA^{+x} + bB^{-y} \rightarrow A_aB_b \tag{1}$$

While pellets continue to grow during the operation, the variations of pellet size, bed voidage and bed height in stage
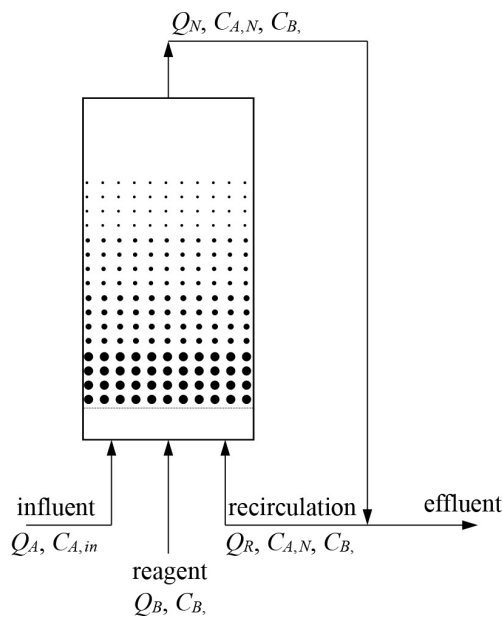

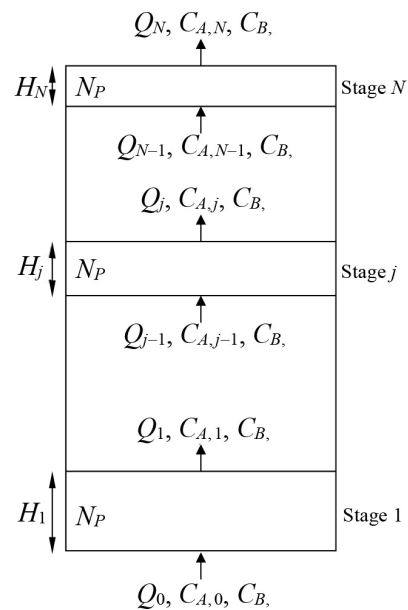Fig. 1. A typical fluidized bed pellet reactor.

Fig. 2. Schematic diagram of a fluidized bed within an FBPR.

j (j = 1, 2, …, N) need to be derived. The mass balance of the two ions, A^{+x} and B^{-y}, in stage j can be respectively described as (Fig. 2):

$$\frac{d}{dt}\left(SH_j\,\varepsilon_j\,C_{A,j}\right) = Q_{j-1}C_{A,j-1} - Q_j C_{A,j} - \frac{1}{2}N_P\,\rho_P\,\pi L_j^2 G_j\,\frac{a}{aM_A + bM_B}$$

(2)

$$\frac{d}{dt}\left(SH_j\,\varepsilon_j\,C_{B,j}\right) = Q_{j-1}C_{B,j-1} - Q_j C_{B,j} - \frac{1}{2}N_P\,\rho_P\,\pi L_j^2 G_j\,\frac{b}{aM_A + bM_B}$$

(3)

where $SH_j\varepsilon_j$ denotes the volume of the liquid phase in stage j and aM_A+bM_B is the molecular weight of A_aB_b. The terms on the left-hand side of Eqs. (2) and (3) are, respectively, the rate of cation and anion accumulation in stage j. The first and second terms on the right-hand side of Eqs. (2) and (3) indicate the inlet and outlet ion molar flow rates in stage j, respectively, and the last term denotes the rate of growth on the surface of the suspended pellets in stage j. The factor 1/2 in the last term of Eqs. (2) and (3) arises because G_j is the growth rate of pellet diameter. The inlet conditions at the entrance of stage 1 can be expressed as:

$$Q_0 = Q_A + Q_B + Q_R$$

(4)

$$C_{A,0} = \frac{Q_A C_{A,\text{in}} + Q_R C_{A,N}}{Q_0}$$

(5)

$$C_{B,0} = \frac{Q_B C_{B,\text{in}} + Q_R C_{B,N}}{Q_0}$$

(6)

where Q_0 is the mixed flow rate of $Q_A+Q_B+Q_R$. Note that Q_A, Q_B, Q_R, $C_{A,\text{in}}$ and $C_{B,\text{in}}$ remain unchanged during the operation. However, as $C_{A,N}$ and $C_{B,N}$ of the recirculation flow vary during the operation, $C_{A,0}$ and $C_{B,0}$ at the entrance of stage 1 also change with the operating time. For convenience, the recirculation ratio is defined as:

$$R = \frac{Q_R}{Q_A + Q_B}$$

(7)

For A_aB_b crystallization (or precipitation) kinetics, the growth rate G_j is generally represented as a power law expression [56]:

$$G_j = \frac{dL_j}{dt} = k_g\left[\left(\frac{C_{A,j}^a C_{B,j}^b}{K_{\text{sp}}}\right)^{\frac{1}{a+b}} - 1\right]^n$$

(8)

where K_{sp} is the solubility product of A_aB_b. Similarly, the mass balance of the solvent (i.e., water) in stage j can be described as:

$$\frac{d}{dt}\left[SH_j\,\varepsilon_j\right] = Q_{j-1} - Q_j$$

(9)

Here it is assumed that the volume of solutes in the solution can be neglected. It should be noted that Eqs. (2), (3) and (9) have stated that the volume of stage j varies with the operating time. By substituting Eq. (9) into Eqs. (2) and (3), to eliminate Q_j, one obtains:

$$\frac{dC_{A,j}}{dt} = \frac{1}{SH_j\,\varepsilon_j}\left[Q_{j-1}\left(C_{A,j-1} - C_{A,j}\right) - \frac{1}{2}N_P\,\rho_P\,\pi L_j^2\,\frac{a}{aM_A + bM_B}\frac{dL_j}{dt}\right]$$

(10)

$$\frac{dC_{B,j}}{dt} = \frac{1}{SH_j\,\varepsilon_j}\left[Q_{j-1}\left(C_{B,j-1} - C_{B,j}\right) - \frac{1}{2}N_P\,\rho_P\,\pi L_j^2\,\frac{b}{aM_A + bM_B}\frac{dL_j}{dt}\right]$$

(11)

As the pellets in stage j grow, the local voidage of stage j will vary with the operating time. In practice, Richardson and Zaki [57] equation is often adopted to describe the expansion characteristic of the fluidized bed:

$$u_s = u_{i,j}\varepsilon_j^{z_j}$$

(12)

$$u_{i,j} = u_{t,j}10^{-L_j/D}$$

(13)

where u_s is the superficial velocity of the solution and $u_{t,j}$ is the terminal free-fall velocity of the particles of size L_j placed in the column of diameter D. The superficial velocity normally lies between terminal velocity and minimum fluidization velocity. The expansion index z_j is a function of $\text{Re}_{t,j}$ and is given by:

$$z_j = \begin{cases} \left(4.4 + 18\frac{L_j}{D}\right)\text{Re}_{t,j}^{-0.1} & 1 < \text{Re}_{t,j} < 200 \\ 4.4\,\text{Re}_{t,j}^{-0.1} & 200 < \text{Re}_{t,j} < 500 \\ 2.4 & \text{Re}_{t,j} > 500 \end{cases}$$

(14)

$$\text{Re}_{t,j} = \frac{u_{t,j}\rho L_j}{\mu}$$

(15)

The term $u_{t,j}$ in Eqs. (13) and (15) is the terminal free-fall velocity of crystals of size L_j which can be evaluated as follows [58]:

$$u_{t,j} = \begin{cases} \dfrac{g\left(\rho_e - \rho\right)L_j^2}{18\,\mu} & \text{Re}_{t,j} < 0.4 \\ \left[\dfrac{4}{225}\dfrac{\left(\rho_e - \rho\right)^2 g^2}{\rho\mu}\right]^{\frac{1}{3}}L_j & 200 < \text{Re}_{t,j} < 500 \\ \left[\dfrac{3.1g\left(\rho_e - \rho\right)L_j}{\rho}\right]^{\frac{1}{2}} & 500 < \text{Re}_{t,j} < 200000 \end{cases}$$

(16)

where ρ_e is the effective density of an A_aB_b-covered particle (Fig. 3) and is defined as:

$$\rho_e = \left(\frac{L_0}{L_j}\right)^3 \rho_S + \left[1 - \left(\frac{L_0}{L_j}\right)^3\right]\rho_P \tag{17}$$

For instance, $u_{t,j}$ lies between 0.0327 and 0.1635 m/s and $Re_{t,j}$ lies between 6.54 and 163.5 for particles of $\rho_e = 2{,}600$ kg/m³ and size 200–1,000 μm suspended in a dilute aqueous solution. Assuming theses ranges of values and differentiating Eqs. (12)–(16) with respect to t gives:

$$\frac{d\varepsilon_j}{dt} = -\frac{\varepsilon_j}{z_j}\left(\frac{1}{u_{i,j}}\frac{du_{i,j}}{dt} + \ln\varepsilon_j \frac{dz_j}{dt}\right) \tag{18}$$

$$\frac{1}{u_{i,j}}\frac{du_{i,j}}{dt} = \frac{1}{u_{t,j}}\frac{du_{t,j}}{dt} - \frac{\ln 10}{D}\frac{dL_j}{dt} \tag{19}$$

$$\frac{dz_j}{dt} = 18\frac{Re_{t,j}^{-0.1}}{D}\frac{dL_j}{dt} - \left(0.44 + 1.8\frac{L_j}{D}\right)Re_{t,j}^{-1.1}\frac{dRe_{t,j}}{dt} \tag{20}$$

$$\frac{dRe_{t,j}}{dt} = \frac{\rho}{\mu}\left(L_j\frac{du_{t,j}}{dt} + u_{t,j}\frac{dL_j}{dt}\right) \tag{21}$$

$$\frac{du_{t,j}}{dt} = \left[\frac{4}{225}\frac{(\rho_e - \rho)^2 g^2}{\rho\mu}\right]^{1/3}\frac{dL_j}{dt} \tag{22}$$

Substituting Eqs. (19–22) into Eq. (18) yields:

$$\frac{d\varepsilon_j}{dt} = \frac{\varepsilon_j}{z_j}\left\{\begin{array}{l} \dfrac{\ln 10}{D} - \dfrac{1}{L_j} \\ + \ln\varepsilon_j\left[\dfrac{\rho u_{t,j} Re_{t,j}^{-1.1}}{\mu}\left(0.88 + 3.6\dfrac{L_j}{D}\right) - 18\dfrac{Re_{t,j}^{-0.1}}{D}\right]\end{array}\right\}\frac{dL_j}{dt} \tag{23}$$

The above equation determines the local voidage of stage j as a function of the operating time. As the local voidage varies, the local bed height of stage j can be calculated by:
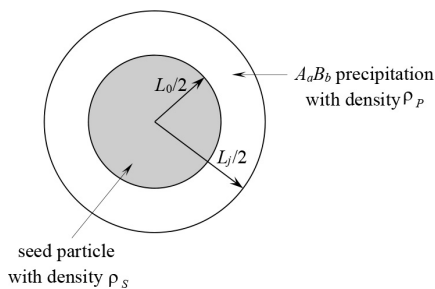

Fig. 3. A pellet with A_aB_b precipitating on the surface.

$$H_j = \frac{N_P \pi L_j^3}{6S(1-\varepsilon_j)} \tag{24}$$

It should be noted that $SH_j(1-\varepsilon_j)$ is the volume of the solid phase in stage j, which equals $N_P\pi L_j^3/6$, the total volume of pellets in stage j. Differentiating H_j in Eq. (24) with respect to t gives:

$$\frac{dH_j}{dt} = \frac{1}{S(1-\varepsilon_j)}\left(SH_j\frac{d\varepsilon_j}{dt} + \frac{\pi}{2}N_P L_j^2\frac{dL_j}{dt}\right) \tag{25}$$

Eqs. (8), (10), (11), (23), and (25) can be solved simultaneously by numerical methods to determine L_j, $C_{A,j}$, $C_{B,j}$, ε_j, and H_j for stage j as a function of the operating time. Note that the solution flow rate Q_{j-1} in Eqs. (10) and (11), which varies with the stage number and the operating time, needs to be determined using Eq. (9). At $t = 0$, the values of $(L_j$, $C_{A,j}$, $C_{B,j}$, H_j, $\varepsilon_j)$ are set to be $(L_0$, $C_{A,0}$, $C_{B,0}$, H_0/N, $\varepsilon_0)$, where H_0/N is the initial bed height of each stage at the start of a run. The initial values of ε_0 and H_0 can be calculated by using Eqs. (12)–(16) and (24) when the seed size and the liquid superficial velocity are given. In this work, the differential equations are solved in MATLAB using the routine ode45.

3. Case studies

3.1. Recovery of nickel as nickel carbonate

The simulation results of an FBPR are presented below to demonstrate the application of the developed model. The process of the Ni²⁺-containing wastewater mixed with the CO_3^{-2}-containing reagent stream in an FBPR will be discussed. Here, we assume that the component precipitating on the pellet surface is only nickel carbonate by controlling the pH of the solution into the FBPR. The conditions employed in the example and the kinetic parameters are listed in Table 1. The value of the growth rate constant k_g is taken from Lee [59]. For the seed particles of density 2,600 kg/m³ and size 200 μm settling freely in an aqueous solution, Re_t equals 6.54 and u_t equals 0.0327 m/s. The superficial velocity is determined by Q_0/S, and u_s is equal to 0.0214 m/s at $R = 100$. It should be noted that the value of u_s must be kept below the value of u_t to avoid carry-over of solids from the bed.

As pellets grow at different rates in different stages during the operation, the pellets in the fluidized bed exhibit a particle size distribution. The total mass of nickel carbonate in the pellets can be expressed by:

$$W_t - W_0 = \sum_{j=1}^{N}\frac{\pi}{6}N_P\left(L_j^3 - L_0^3\right)\rho_P \tag{26}$$

where W_t is the total pellet mass which increases with the operating time and W_0 is the total seed mass. In Fig. 4, $(W_t - W_0)/W_0$ and H_t/H_0 are plotted against the operating time at $C_{A,\text{in}} = 0.03$ M, $C_{B,\text{in}} = 0.09$ M and $R = 100$. As shown in the figure, the total bed height (H_t), which determines the size of the reactor, increases with the operating time and reaches

about 1.16 times of the original bed height after 50-h operation. In practice, the operation period of an FBPR may last for several weeks; thus, the increase of the total bed height can be quite significant and needs to be carefully considered in the design of an FBPR. It should be noted that the total mass of nickel carbonate in the pellets increases up to 60% after 50 h of operation.

Figs. 5–7 show, respectively, the variations of the Ni^{2+} concentration, the pellet size and the bed voidage with the vertical position within the FBPR for various operating times at $C_{A, in} = 0.03$ M, $C_{B, in} = 0.09$ M and $R = 100$. In Fig. 5, $C_A/C_{A, in}$ is a monotonic decreasing function of H/H_t for several operating times. As the inlet nickel ion is treated with the

Table 1
Conditions employed in the nickel carbonate example

Parameter	Value
L_0, μm	200
N_t	3×10^7
W_0, kg	0.3267
D, m	0.06
n in Eq. (5)	0.914[a]
k_g in Eq. (5), m/s	1.6462×10^{-11}[a]
Q_A, m³/s	3×10^{-7}
Q_B, m³/s	3×10^{-7}
$C_{A, in}$, M	0.03
K_{sp}, M²	6.6×10^{-9}
μ, kg/m/s	1×10^{-3}
ρ, kg/m³	1,000
ρ_P, kg/m³	2,600
ρ_s, kg/m³	2,600
N	40
Δt, s	0.1
t_s, h	50

[a]Data from a study by Lee [59].
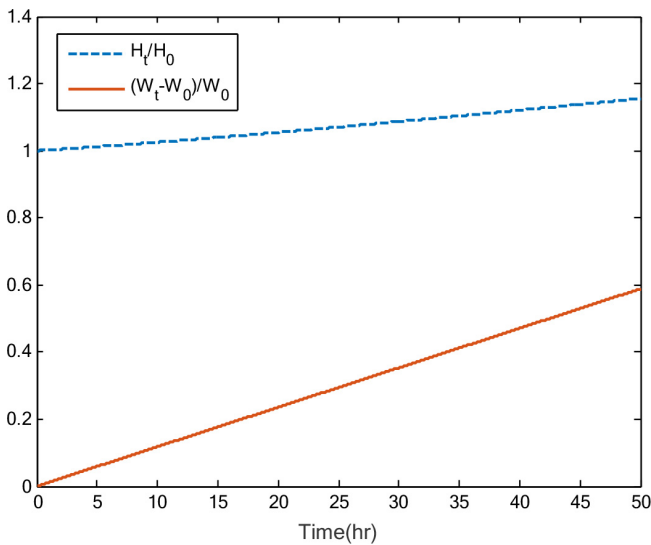
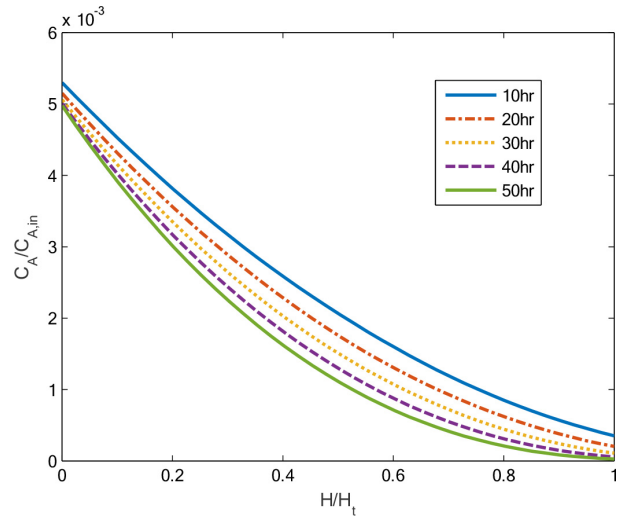Fig. 4. Total bed height and weight of precipitate vs. time for the nickel carbonate system

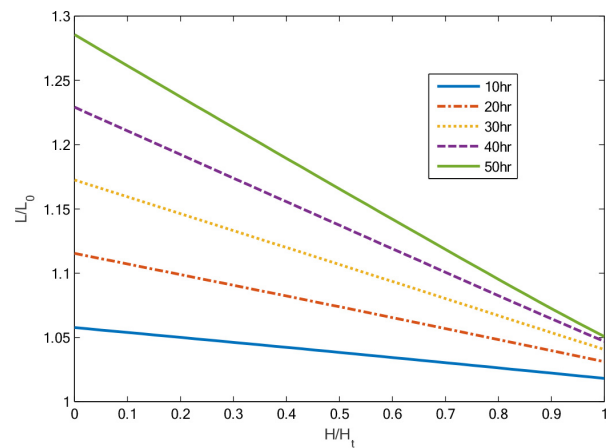Fig. 5. Relative concentration of Ni^{2+} at different positions.

Fig. 6. Relative seed diameter of $NiCO_3$ pellets vs. position at different times.
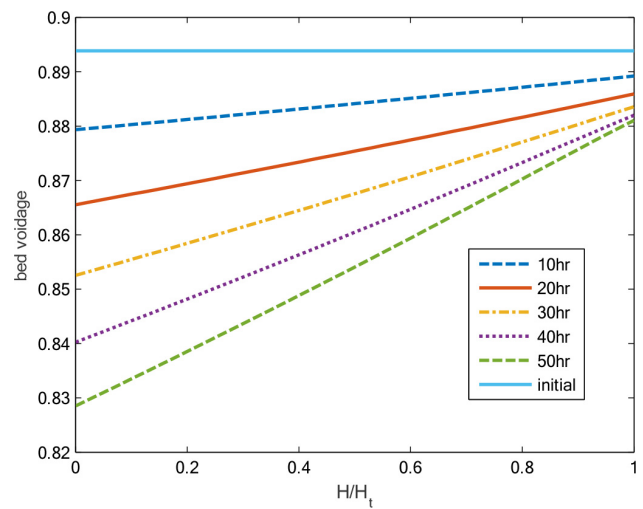

Fig. 7. Bed voidage vs. position for $NiCO_3$ system at different times.

carbonate-containing reagent to form $NiCO_3$ precipitation on the pellets surface, the Ni^{2+} concentration decreases along the upward flow direction of the bed. Due to the dilution effect of the recirculation flow, the mixed Ni^{2+} concentration at the bottom of the FBPR drops during the operation. Then, the decrease of Ni^{2+} concentration along the bed height follows the similar pattern at several operating times. In addition, as the pellets grow larger and the overall surface areas of pellets available for pellet growth become larger, the effluent Ni^{2+} concentration also decreases during the operation, as shown in Fig. 5. In Fig. 6, the pellet size decreases monotonically with the bed height for selected operating times. It is obvious that the pellet size increases with time at any position of the bed. Also, one can see that the variation of the pellet sizes within the bed increases as the operating time is increased. It can be seen in Fig. 7 that the voidage of the bed increases monotonically with H/H_t. The value of initial voidage ε_0 (=0.894) is exhibited by the dotted line. As indicated in Fig. 7, the bed voidage drops faster with the operating time at the lower part than that at the upper part of the bed. For instance, the bed voidage drops slightly from 0.894 to 0.881 at the top while the bed voidage at the bottom is reduced from 0.894 to 0.829 after 50-h operation.

Fig. 8 shows the Ni^{2+} concentration vs. position in the bed after 50 h for three different seed masses. As expected, if the seed mass is increased, the Ni^{2+} ion concentration decreases. If the seed mass is doubled, the effluent concentration has nearly reached the equilibrium concentration at a position 60% of the distance from the bottom to the top of the bed.

Fig. 9 shows the effect of the recycle ratio R on the Ni^{2+} ion concentration profile. Increase in recycle ratio increases mixing, which decreases the ion concentration at the bottom of the bed but increases the concentration near the top of the bed.

Figs. S1–S4 in the supplement show additional results for the nickel carbonate case study. Figs. S1 and S2 show the effect of changing the bed diameter. The relative concentration profile and relative particle size profile remain unchanged because the kinetic model for the nickel carbonate crystals

predicts that the crystal growth rate does not depend on the fluid superficial velocity. If the bed diameter is increased, then the bed height and superficial velocity are decreased, but the relative concentration and particle size are unaffected.

Fig. S3 shows the effect of recycle ratio on particle size distribution. Because of the mixing effect, as the recycle ratio increases the bed becomes less stratified, that is, the difference in particle size between the top and bottom of the bed decreases. Fig. S4 shows the effect of changing the feed concentration of reagent on the Ni^{2+} ion concentration profile. If the feed concentration ratio is reduced to 1, the concentration across the bed is significantly increased because the driving force for crystallization is substantially reduced. An excess of reagent ion (CO_3^{2-}) can reduce the Ni^{2+} ion concentration dramatically.

3.2. Removal of fluoride as calcium fluoride

As a second example, consider the removal of fluoride ions from wastewater. Calcium fluoride is sparingly soluble in water ($K_{SP} = 3.4 \times 10^{-11} M^2$) and so

Aldaco et al. [60] provided the following kinetic model for the growth rate of calcium fluoride crystals in a pellet reactor:

$$G_j = 2.96 \times 10^{-5} L_0^{1.37} u_s^{0.49} S^{1.02} \tag{27}$$

where S denotes supersaturation, which is defined as:

$$S = \left(\frac{\left[Ca^{2+} \right]\left[F^- \right]^2}{K_{sp}} \right)^{1/3} - 1 \tag{28}$$

Tables 2 and 3 show the physical properties and base-case process properties, respectively, for the calcium fluoride process.
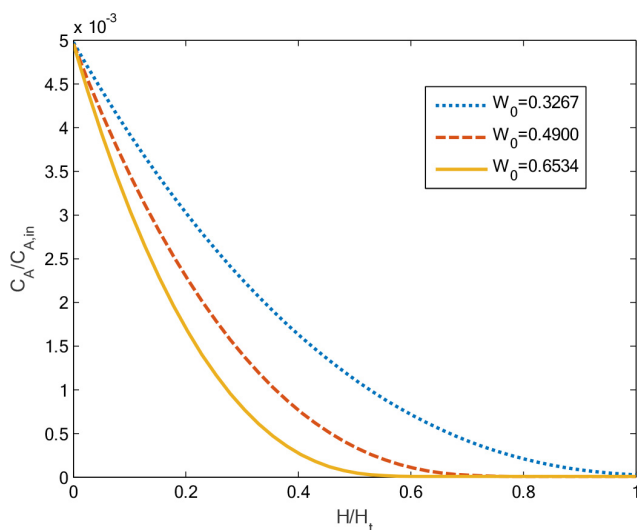

Fig. 8. Concentration vs. position for three different seed pellet loadings.
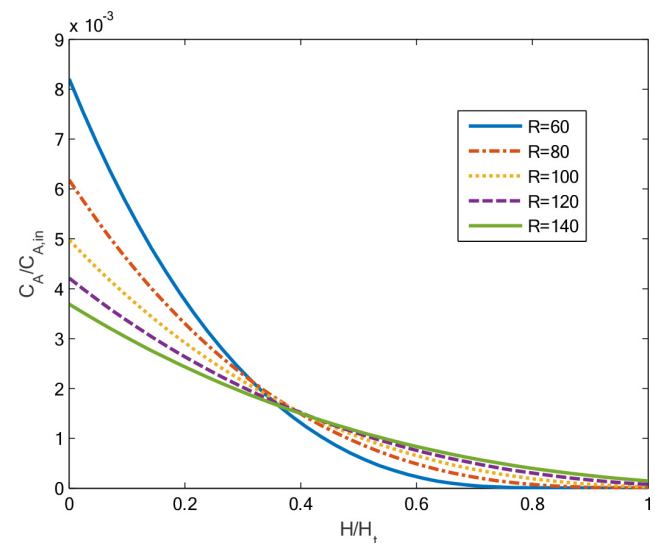

Fig. 9. Nickel concentration vs. position for different values of the recycle ratio.

Table 2
Physical properties for calcium fluoride

Symbol	Value
a	1
b	2
M_A, g/mol	40.078
M_B, g/mol	18.998
K_{sp}, M^2	3.4×10^{-11}
ρ, kg/m^3	1,000
ρ_p, kg/m^3	3,180
ρ_s, kg/m^3	2,710
μ, Pa·S	1.0×10^{-3}
k_g, m/s	2.96×10^{-5}
n	1.02

Table 3
Experimental and initial conditions for calcium fluoride system

Symbol	Value
L_0, μm	425
N_t	642,630
W_0, kg	0.07
D, m	0.02
Q_A, m^3/s	1.15×10^{-6}
Q_B, m^3/s	1.72×10^{-6}
$C_{A,in}$, M	0.00374
$C_{B,in}$, M	0.007896
N	40
t_s, h	50
R	0

Fig. 10 shows the relative bed height and seed pellet mass over 50 h of operation. As with the nickel carbonate process, both rise steadily during the batch as mass is deposited on the pellets and they grow larger. Fig. 11 shows the concentration of fluoride ion vs. position in the reactor at different times. As for the nickel carbonate case, the outlet concentration gradually decreases during the batch as the pellet size (and therefore surface area) increases. The outlet concentration of fluoride ion is greater than that of nickel concentration because of differences in the kinetic rate expression, equilibrium concentration and feed concentrations. The design of a process that can achieve a desired contaminant outlet concentration are given in Section 4.

Figs. S5 and S6 in the supplement show the relative pellet diameter and bed voidage profiles, respectively, for the calcium fluoride process at different times after the start of the batch. Figs. S7 and S8 show the relative fluoride ion concentration and particle diameter respectively vs. relative position in the bed for different seed masses. Figs. S9 and S10 show the effect of changing the bed diameter. Because the crystal growth rate is a function of fluid velocity for the calcium fluoride process (Eq. (27)) the bed diameter has a significant effect on the profiles. When the bed diameter is smaller, the superficial velocity is greater, and therefore the predicted crystal growth rate is also larger.
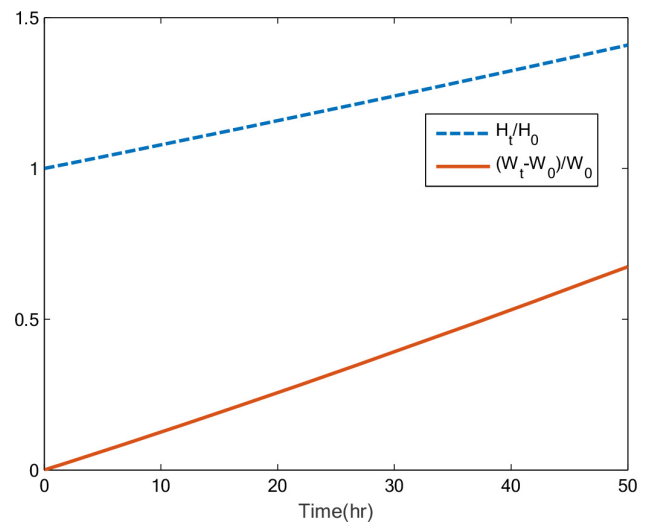

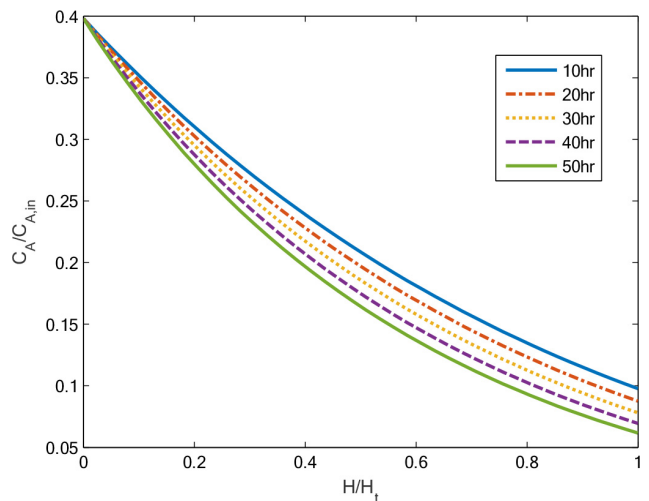Fig. 10. Bed height and net pellet mass vs. time for the calcium fluoride system.

Fig. 11. Fluoride concentration vs. bed position at different times for the calcium fluoride system.

Figs. S11 and S12 show the effect of changing the recycle ratio. As for the nickel carbonate process, increasing the recycle ratio increases the mixing in the process; however, it also increases the bed superficial velocity, leading to a greater crystal growth rate. Therefore, the outlet concentration of fluoride ion decreases and pellet size increases as the recycle ratio increases. Finally, Figs. S13 and S14 show the effect of changing the reagent concentration. As the calcium concentration in the reagent feed increases, the fluoride concentration decreases and the pellet size increases.

3.3. Removal of ammonium and phosphate as struvite (magnesium ammonium phosphate, MgNH$_4$PO$_4$)

As a final example, the removal of ammonium and phosphate as struvite (magnesium ammonium phosphate) is considered. Ammonium and phosphate are found in wastewater from farms as well as the food and beverage

industries. Discharging water rich in these nutrients into the environment can cause eutrophication. Ali and Schneider [11] presented the following kinetic model for the growth of struvite crystals:

$$\frac{dL}{dt} = \left(46.64 \pm 8.026\right) S^{1.48 \pm 0.162} \tag{29}$$

For the struvite process, ions are identified as follows: $A = Mg^{2+}$, $B = NH_4^+$, $C = PO_4^{3-}$. Tables 4 and 5 show the physical properties and base-case process conditions, respectively, for the struvite process.

Fig. 12 shows the relative values of the bed height and solid pellet mass during a batch. Because somewhat smaller pellets are used in the struvite process and because there are two contaminant ions which precipitate out of solution, the bed height more than doubles and the pellet mass more than triples after only 10 h. Therefore, this shorter batch time is adopted for the struvite process. Fig. 13 shows the phosphate ion concentration vs. position in the bed for different times, and Fig. 14 shows the pellet height vs. position at different times. Fig. S15

Table 4
Physical properties of struvite

Symbol	Value
a	1
b	1
c	1
M_A, g/mol	24.305
M_B, g/mol	18.038
M_C, g/mol	94.971
K_{sp}, M^3	7.08×10^{-14}
ρ, kg/m^3	1,000
ρ_p, kg/m^3	1,700
ρ_s, kg/m^3	1,700
μ, Pa·s	1.0×10^{-3}
k_g, m/s	46.64
n	1.48

Table 5
Experimental and initial conditions for struvite system

Symbol	Value
L_0, μm	140
N_t	1×10^6
W_0, kg	0.0024
D, m	0.08
Q_A, m^3/s	2.78×10^{-7}
Q_B, m^3/s	2.78×10^{-7}
$C_{A,in}$, M	0.005
$C_{B,in}$, M	0.005
$C_{C,in}$, M	0.005
N	40
t_s, h	10
R	50

in the supplement shows the bed voidage vs. bed height for different times after the start of the batch. Figs. S16 and S17 show the dimensionless outlet concentration and pellet size profiles after 10 h for different bed diameters. Since the crystal growth rate model does not predict any dependence of the crystal growth rate on the solution superficial velocity, the curves overlap as was the case for the nickel carbonate system.

4. Reactor design procedure

4.1. General design procedure

The process model described in this work can be used either to model an existing FBPR or as part of a design procedure. In this section, a systematic design procedure for an FBPR based on the model is presented. The procedure is shown schematically in Fig. 15. The procedure begins with the specification of the seed size (L_0), the volumetric flow rate
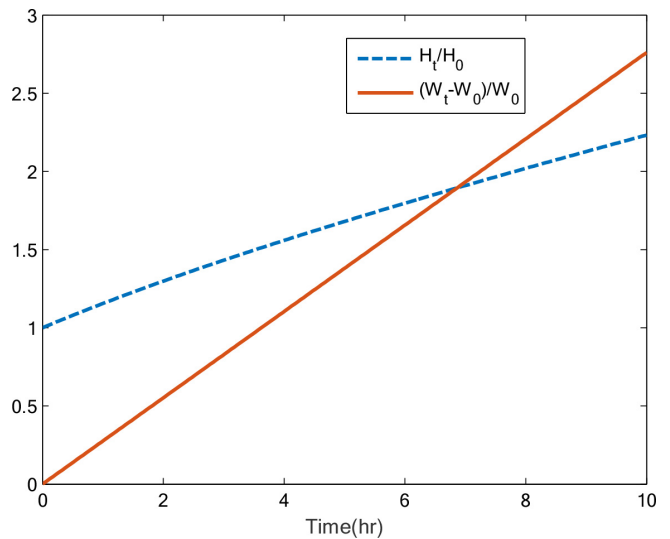

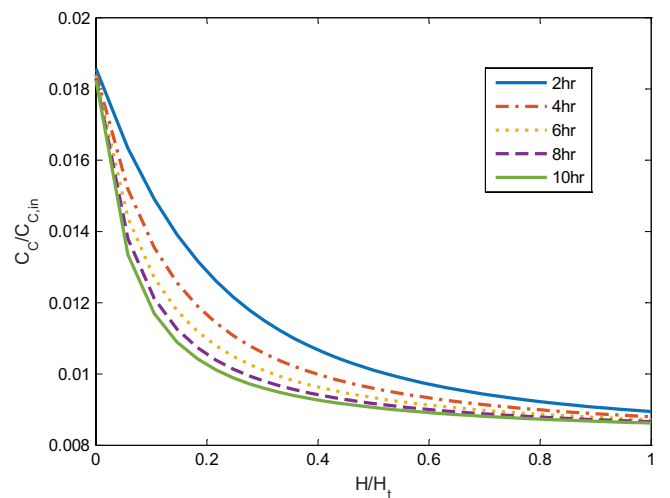Fig. 12. Bed height and net pellet mass vs. time for the struvite system.

Fig. 13. Phosphate concentration vs. position for different values of the recycle ratio.
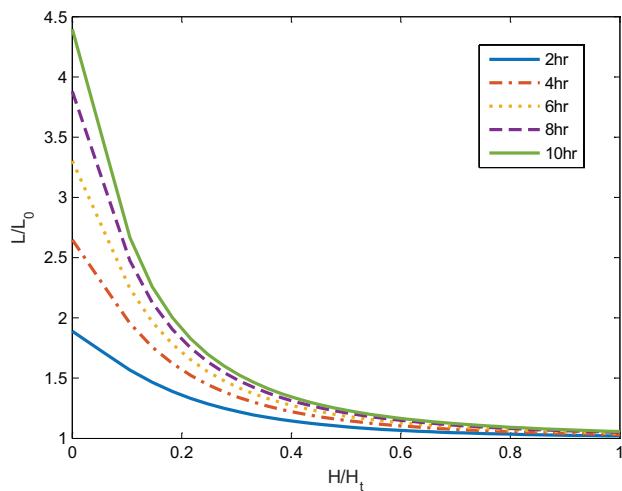
Fig. 14. Seed diameter vs. position for at different times for the struvite system.
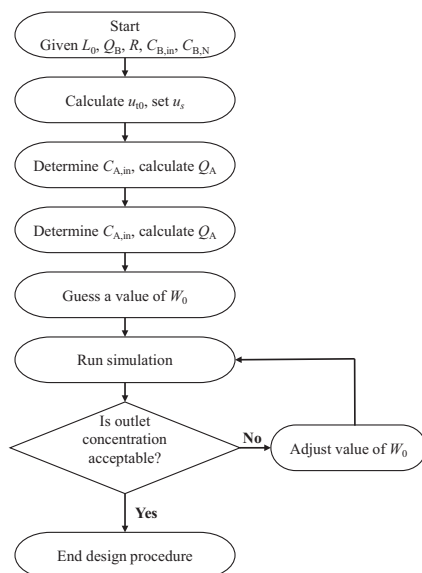

Fig. 15. Flowchart for FBPR design.

of the contaminated wastewater (Q_B), the recycle rate R, and the inlet and desired outlet concentrations of the contaminant ($C_{B,in}$ and $C_{B,out}$, respectively).

Next, knowing the density and size of the seed particles, the single particle terminal velocity can be calculated. Then a reasonable value of the superficial velocity can be determined in order to ensure that the bed is fully fluidized but no particles are entrained in the liquid. Next the concentration of the reagent can be determined from the solubility of the reagent in water, and the volumetric flow rate of reagent solution can be determined based on the reagent concentration, the desired contaminant outlet concentration, and the product solubility constant. Next the bed diameter can be determined given the volumetric flow rates and superficial velocity. Finally, an initial guess is made for the initial pellet mass. The model can then be run and the outlet concentration can be checked against the desired outlet concentration. If the

Table 6
Parameters for FBPR process design

Symbol	Value
R	10
$C_{B,in}$, mg/L	500
Q_B, m³/h	0.001
L_0, μm	200

outlet concentration exceeds the desired outlet concentration, the seed pellet mass can be increased until the desired outlet concentration is achieved.

4.2. Illustration of design procedure

As an example, consider the treatment of wastewater containing 500 mg/L fluoride ion. Suppose it is desired to reduce the outlet concentration to 5 mg/L. Additional parameters for the design are given in Table 6.

First, the single pellet terminal velocity is calculated from Eq. (16): $u_{t,0}$ = 0.0342 m/s. The superficial velocity is set to be 60% of the terminal velocity because this velocity should be greater than the minimum fluidization velocity but less than the terminal velocity over the entire batch. The reagent is taken to be calcium hydroxide Ca(OH)$_2$ with a concentration of 0.01M. Assuming that the outlet concentration of calcium fluoride is nearly in equilibrium with the solid and knowing the solubility product constant, the required inlet flow rate of calcium hydroxide solution can be determined. Finally, knowing the feed flow rates of both streams, the recycle ratio and the superficial velocity, the bed diameter can be determined.

There is one remaining unknown parameter, which is the mass of seed pellets. A suitable mass of seed pellets can be found by simulating the process operation for different values of the seed mass. The results of such simulation are shown in Fig. S18. When a seed mass of 350 g is used, the dimensionless fluoride ion concentration drops below 0.01 after 50 h. Finally, after the seed mass is determined, the bed height at the end of the batch can be calculated. The actual reactor height is set to be 20% larger than the maximum bed height to allow for settlement of entrained particles and for a margin of error.

5. Conclusions

This paper presents a mathematical model for the simulation of an FBPR. The model consists of a series of coupled ordinary differential equations and accounts for variation in pellet size and reagent and contaminant concentration with axial position in the reactor. The model was applied to three relevant problems in industrial wastewater treatment: recovery of nickel as nickel carbonate, removal of fluoride as calcium fluoride, and removal of ammonium and phosphate as struvite. The model is useful for understanding the behavior of FBPRs and the effect of modifying design parameters on the performance of the reactor. A process design procedure based on the model is also proposed and illustrated with an example of a process to produce an FBPR for removal of fluoride from wastewater.

Symbols

a	—	Number of A in the molecule A_aB_b
b	—	Number of B in the molecule A_aB_b
$C_{A,0}$	—	Concentration of A^{+x} in the mixed flow of Q_0 given by Eq. (5), kmol/m³
$C_{A,\text{in}}$	—	Concentration of A^{+x} in the influent, kmol/m³
$C_{A,j}$	—	Concentration of A^{+x} in stage j, kmol/m³
$C_{A,N}$	—	Concentration of A^{+x} in stage N, that is, the effluent concentration of A^{+x}, kmol/m³
$C_{B,0}$	—	Concentration of B^{-y} in the mixed flow of Q_0 given by Eq. (6), kmol/m³
$C_{B,\text{in}}$	—	Concentration of B^{-y} in the reagent stream, kmol/m³
$C_{B,j}$	—	Concentration of B^{-y} in stage j, kmol/m³
$C_{B,N}$	—	Concentration of B^{-y} in stage N, that is, the effluent concentration of B^{-y}, kmol/m³
D	—	Diameter of the bed, m
g	—	9.8 m/s², gravity acceleration
G_j	—	Growth rate of pellets in stage j, m/s
H	—	Vertical position from the bottom of the bed, m
H_0	—	Total bed height at the start of a run, m
H_j	—	Bed height of stage j, m
H_t	—	Total bed height at time t $(=\sum_{j=1}^{N}H_j)$, m
k_g	—	Constant in Eq. (5), m/s
K_{sp}	—	Solubility product of A_aB_b, (kmol/m³)³ᵃ⁺ᵇ
L	—	Pellet diameter, m
L_0	—	Seed diameter, m
L_j	—	Pellet diameter in stage j, m
M_A	—	Molecular weight of A in the molecule A_aB_b, kg/kmol
M_B	—	Molecular weight of B in the molecule A_aB_b, kg/kmol
n	—	Constant in Eq. (5)
N	—	Number of stages in the bed
N_P	—	Number of pellets in each stage $(=N_t/N)$
N_t	—	Total number of seeds
Q_0	—	Mixed flow rate of $Q_A+Q_B+Q_R$ at the entrance of stage 1, m³/s
Q_A	—	Flow rate of the A^{+x}-containing influent, m³/s
Q_B	—	Flow rate of the B^{-y}-containing reagent stream, m³/s
Q_j	—	Outlet flow rate of the solution from stage j, m³/s
Q_R	—	Recirculation flow rate, m³/s
R	—	Recirculation ratio given by Eq. (4)
$\text{Re}_{t,j}$	—	Reynolds number given by Eq. (11)
S	—	Cross section area of the bed, m²
t	—	Operating time, s
t_s	—	Duration of a batch operation, s
u_s	—	Superficial velocity, m/s
$u_{i,j}$	—	Velocity given by Eq. (9), m/s
$u_{t,j}$	—	Terminal velocity of pellets in stage j, m/s
W_0	—	Total mass of seeds $(= N_t \pi L_0^3 \rho_S / 6)$, kg
W_t	—	Total mass of pellets at time t, kg
x	—	Charge number of A^{+x}
y	—	Charge number of B^{-y}
z_j	—	Expansion index given by Eq. (10)

Greeks

ε_0	—	Initial bed voidage
ε_j	—	Bed voidage of stage j
μ	—	Viscosity of the solution, kg/m/s
ρ	—	Density of the solution, kg/m³
ρ_e	—	Effective density of the A_aB_b-covered pellet, kg/m³
ρ_P	—	Density of the precipitation A_aB_b, kg/m³
ρ_S	—	Density of the seed, kg/m³

References

[1] A. Graveland, J.C. Vandijk, P.J. Demoel, J. Oomen, Developments in water softening by means of pellet reactors, J. AWWA, 75 (1983) 619–625.

[2] M. van Ammers, J.C. van Dijk, A. Graveland, P.A.N.M. Nühn, State of the art of pellet softening in the Netherlands, Water Supply, 4 (1986) 223–235.

[3] C.Y. Tai, W.C. Chien, C.Y. Chen, Crystal growth kinetics of calcite in a dense fluidized-bed crystallizer, AIChE J., 45 (1999) 1605–1614.

[4] C.Y. Tai, M.C. Chang, C.K. Wu, Y.C. Lin, Interpretation of calcite growth data using the two-step crystal growth model, Chem. Eng. Sci., 61 (2006) 5346–5354.

[5] W.N. Al Nasser, F.H. Al Salhi, Kinetics determination of calcium carbonate precipitation behavior by inline techniques, Powder Technol., 270 (2015) 548–560.

[6] R.Z. Hu, T.L. Huang, G. Wen, S.Y. Yang, Modelling particle growth of calcium carbonate in a pilot-scale pellet fluidized bed reactor, Water Sci. Technol.-Water Supply, 17 (2017) 643–651.

[7] C. van der Veen, A. Graveland, Central softening by crystallization in a fluidized-bed process, J. AWWA, 80 (1988) 51–58.

[8] J.C. van Dijk, H. Braakensiek, Phosphate removal by crystallization in a fluidized bed, Water Sci. Technol., 17 (1985) 133–142.

[9] L. Montastruc, S. Domenech, L. Pibouleau, C. Azzaro-Pantel, Methodology of study and modelization of dephosphorization of aqueous effluents, Can. J. Chem. Eng., 83 (2005) 742–754.

[10] L. Montastruc, S. Domenech, L. Pibouleau, C. Azzaro-Pantel, Experimental validation of calcium phosphate precipitation modeling in a pellet reactor, Environ. Technol., 26 (2005) 683–693.

[11] M.I. Ali, P.A. Schneider, An approach of estimating struvite growth kinetic incorporating thermodynamic and solution chemistry, kinetic and process description, Chem. Eng. Sci., 63 (2008) 3514–3525.

[12] M. Iqbal, H. Bhuiyan, D.S. Mavinic, Assessing struvite precipitation in a pilot-scale fluidized bed crystallizer, Environ. Technol., 29 (2008) 1157–1167.

[13] M.I.H. Bhuiyan, D.S. Mavinic, R.D. Beckie, Nucleation and growth kinetics of struvite in a fluidized bed reactor, J. Cryst. Growth, 310 (2008) 1187–1194.

[14] X. Ye, Z.L. Ye, Y.Y. Lou, S.Q. Pan, X.J. Wang, M.K. Wang, S.H. Chen, A comprehensive understanding of saturation index and upflow velocity in a pilot-scale fluidized bed reactor for struvite recovery from swine wastewater, Powder Technol., 295 (2016) 16–26.

[15] Y.J. Shih, R.R.M. Abarca, M.D.G. de Luna, Y.H. Huang, M.C. Lu, Recovery of phosphorus from synthetic wastewaters by struvite crystallization in a fluidized-bed reactor: effects of ph, phosphate concentration and coexisting ions, Chemosphere, 173 (2017) 466–473.

[16] K.S. Le Corre, E. Valsami-Jones, P. Hobbs, S.A. Parsons, Phosphorus recovery from wastewater by struvite crystallization: a review, Crit. Rev. Environ. Sci. Technol., 39 (2009) 433–477.

[17] M.I.H. Bhuiyan, D.S. Mavinic, F.A. Koch, Phosphorus recovery from wastewater through struvite formation in fluidized bed reactors: a sustainable approach, Water Sci. Technol., 57 (2008) 175–181.

[18] C.C. Su, L.D. Dulfo, M.L.P. Dalida, M.C. Lu, Magnesium phosphate crystallization in a fluidized-bed reactor: effects of pH, Mg:P molar ratio and seed, Sep. Purif. Technol., 125 (2014) 90–96.

[19] C. Zhang, K.N. Xu, J.Y. Li, C.W. Wang, M. Zheng, Recovery of phosphorus and potassium from source-separated urine using a fluidized bed reactor: optimization operation and mechanism modeling, Ind. Eng. Chem. Res., 56 (2017) 3033–3039.

[20] P. Zamora, T. Georgieva, I. Salcedo, N. Elzinga, P. Kuntke, C.J.N. Buisman, Long-term operation of a pilot-scale reactor for phosphorus recovery as struvite from source-separated urine, J. Chem. Technol. Biotechnol., 92 (2017) 1035–1045.

[21] E. Eggers, A.H. Dirkzwager, H. Vanderhoning, Full-scale experiences with phosphate crystallization in a crystalactor, Water Sci. Technol., 23 (1991) 819–824.

[22] R. Aldaco, A. Garea, A. Irabien, Fluoride recovery in a fluidized bed: crystallization of calcium fluoride on silica sand, Ind. Eng. Chem. Res., 45 (2006) 796–802.

[23] R. Aldaco, A. Garea, A. Irabien, Calcium fluoride recovery from fluoride wastewater in a fluidized bed reactor, Water Res., 41 (2007) 810–818.

[24] R. Aldaco, A. Irabien, P. Luis, Fluidized bed reactor for fluoride removal, Chem. Eng. J., 107 (2005) 113–117.

[25] A. Garea, R. Aldaco, A. Irabien, Improvement of calcium fluoride crystallization by means of the reduction of fines formation, Chem. Eng. J., 154 (2009) 231–235.

[26] K. Jiang, K.G. Zhou, Y.C. Yang, H. Du, Growth kinetics of calcium fluoride at high supersaturation in a fluidized bed reactor, Environ. Technol., 35 (2014) 82–88.

[27] L.Y. Deng, Y.W. Liu, T.L. Huang, T. Sun, Fluoride removal by induced crystallization using fluorapatite/calcite seed crystals, Chem. Eng. J., 287 (2016) 83–91.

[28] C.Y. Tai, P.C. Chen, T.M. Tsao, Growth kinetics of CaF2 in a pH-stat fluidized-bed crystallizer, J. Cryst. Growth, 290 (2006) 576–584.

[29] M. Schöller, J.C. van Dijk, D. Wilms, Recovery of heavy metals by crystallization in the pellet reactor, Environ. Technol., 8 (1987) 294–303.

[30] P. Zhou, J.C. Huang, A.W.F. Li, S. Wei, Heavy metal removal from wastewater in fluidized bed reactor, Water Res., 33 (1999) 1918–1924.

[31] C.I. Lee, W.F. Yang, Heavy metal removal from aqueous solution in sequential fluidized-bed reactors, Environ. Technol., 26 (2005) 1345–1354.

[32] A.H.M. Veeken, L. Akoto, L. W. Hulshoff Pol, J. Weijma, Control of the sulfide (S²⁻) concentration for optimal zinc removal by sulfide precipitation in a continuously stirred tank reactor, Water Res., 37 (2003) 3709–3717.

[33] J.P. Chen, H. Yu, Lead removal from synthetic wastewater by crystallization in a fluidized-bed reactor, J. Environ. Sci. Health, Part A-Toxic/Hazard. Subst. Environ. Eng., 35 (2000) 817–835.

[34] C.-W. Li, Y.-M. Liang, Y.-M. Chen, Combined ultrafiltration and suspended pellets for lead removal, Sep. Purif. Technol., 45 (2005) 213–219.

[35] M.D.G. de Luna, L.M. Bellotindos, R.N. Asiao, M.-C. Lu, Removal and recovery of lead in a fluidized-bed reactor by crystallization process, Hydrometallurgy, 155 (2015) 6–12.

[36] C. Huang, J.R. Pan, M. Lee, S. Yen, Treatment of high-level arsenic-containing wastewater by fluidized bed crystallization process, J. Chem. Technol. Biotechnol., 82 (2007) 289–294.

[37] C.-I. Lee, W.-F. Yang, C.-I. Hsieh, Removal of Cu(II) from aqueous solution in a fluidized-bed reactor, Chemosphere, 57 (2004) 1173–1180.

[38] N. Boonrattanakij, M.C. Lu, J. Anotai, Iron crystallization in a fluidized-bed Fenton process, Water Res., 45 (2011) 3255–3262.

[39] Y. Shimizu, I. Hirasawa, Effect of seeding on metal ion recovery from wastewater by reactive crystallization of metal carbonates, Chem. Eng. Technol., 35 (2012) 1588–1592.

[40] D. Guillard, A.E. Lewis, Nickel carbonate precipitation in a fluidized-bed reactor, Ind. Eng. Chem. Res., 40 (2001) 5564–5569.

[41] D. Guillard, A.E. Lewis, Optimization of nickel hydroxycarbonate precipitation using a laboratory pellet reactor, Ind. Eng. Chem. Res., 41 (2002) 3110–3114.

[42] V.C.T. Costodes, A.E. Lewis, Reactive crystallization of nickel hydroxy-carbonate in fluidized-bed reactor: fines production and column design, Chem. Eng. Sci., 61 (2006) 1377–1385.

[43] M. Scholler, J.C. van Dijk, D. Wilms, Fluidized bed pellet reactor to recover metals or anions, Met. Finish., 89 (1991) 46–50.

[44] D. Wilms, A. van Haute, J. van Dijk, M. Scholler, Recovery of Nickel by Crystallization of Nickel Carbonate in a Fluidized-bed Reactor, Water Pollution Control in Asia, Pergamon Press, Oxford, 1987.

[45] D. Wilms, K. Vercaemst, J.C. van Dijk, Recovery of silver by crystallization of silver carbonate in a fluidized-bed reactor, Water Res., 26 (1992) 235–239.

[46] L.D. Shiau, T.S. Lu, Interactive effects of particle mixing and segregation on the performance characteristics of a fluidized bed crystallizer, Ind. Eng. Chem. Res., 40 (2001) 707–713.

[47] L. Montastruc, C. Azzaro-Pantel, B. Biscans, M. Cabassud, S. Domenech, L. Dibouleau, A general framework for pellet reactor modelling: application to P-recovery, Chem. Eng. Res. Des., 81 (2003) 1271–1278.

[48] L. Montastruc, C. Azzaro-Pantel, L. Pibouleau, S. Domenech, A systemic approach for pellet reactor modeling: application to water treatment, AIChE J., 50 (2004) 2514–2525.

[49] C.Y. Tai, Crystal growth kinetics of two-step growth process in liquid fluidized-bed crystallizers, J. Cryst. Growth, 206 (1999) 109–118.

[50] K.M. van Schagen, L.C. Rietveld, R. Babuska, O.J. Kramer, Model-based operational constraints for fluidised bed crystallisation, Water Res., 42 (2008) 327–337.

[51] W.D. Jr. Harms, R.B. Robinson, Softening by fluidized bed crystallizers, J. Environ. Eng., 118 (1992) 513–529.

[52] M.M. Seckler, O.S.L. Bruinsma, G.M. van Rosmalen, Phosphate removal in a fluidized bed – I. Identification of physical processes, Water Res., 30 (1996) 1585–1588.

[53] M.M. Seckler, O.S.L. Bruinsma, G.M. van Rosmalen, Calcium phosphate precipitation in a fluidized bed in relation to process conditions: a black box approach, Water Res., 30 (1996) 1677–1685.

[54] M.M. Seckler, M.L.J. van Leeuwen, O.S.L. Bruinsma, G.M. van Rosmalen, Phosphate removal in a fluidized bed – II. Process optimization, Water Res., 30 (1996) 1589–1596.

[55] L.D. Shiau, S.H. Cheng, Y.C. Liu, Modeling of a fluidized-bed crystallizer operated in a batch mode, Chem. Eng. Sci., 54 (1999) 865–871.

[56] A.E. Nielsen, Electrolyte crystal growth mechanism, J. Cryst. Growth, 67 (1984) 289–310.

[57] J.F. Richardson, J.F. Zaki, Sedimentation and fluidization. Part I, Trans. Inst. Chem. Eng., 32 (1954) 35–52.

[58] D. Kunii, O. Levenspiel, Fluidization Engineering, Wiley Press, New York, 1969.

[59] M.S. Lee, The Application of Inorganic Wastewater Treatment with Crystallization Technology in a Fluidized Bed, Master Thesis, Chung Yuan Christian University, Taiwan, R.O.C., 1993.

[60] R. Aldaco, A. Garea, A. Irabien, Modeling of particle growth: application to water treatment in a fluidized bed reactor, Chem. Eng. J., 134 (2007) 66–71.
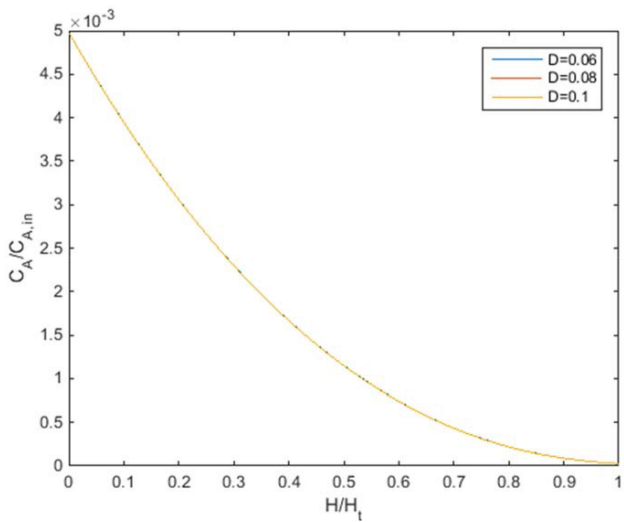
Supplementary material

Fig. S1. Distribution of relative Ni^{2+} concentration for different bed diameters.
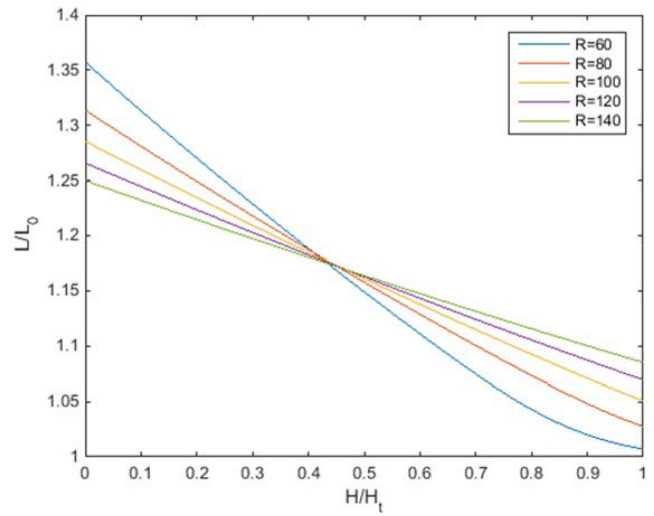

Fig. S3. Distribution of relative NiCO$_3$ seed size for different recycle ratios.
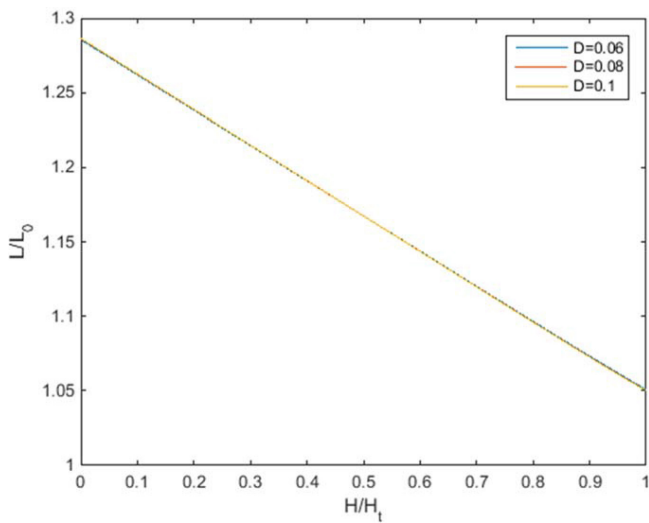

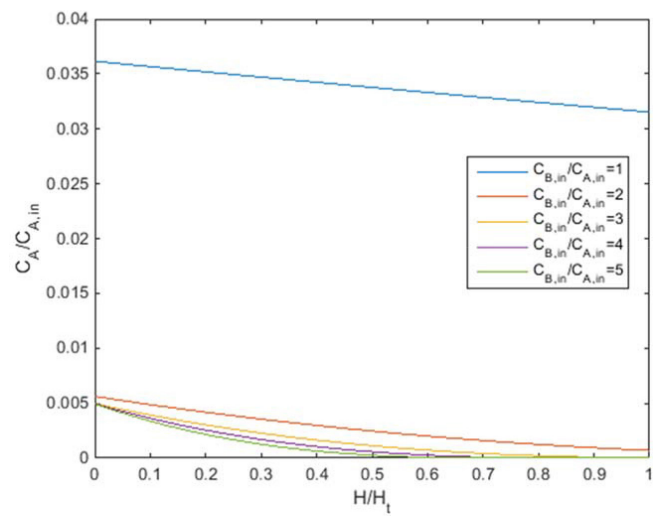Fig. S2. Distribution of relative NiCO$_3$ seed size for different bed diameters.

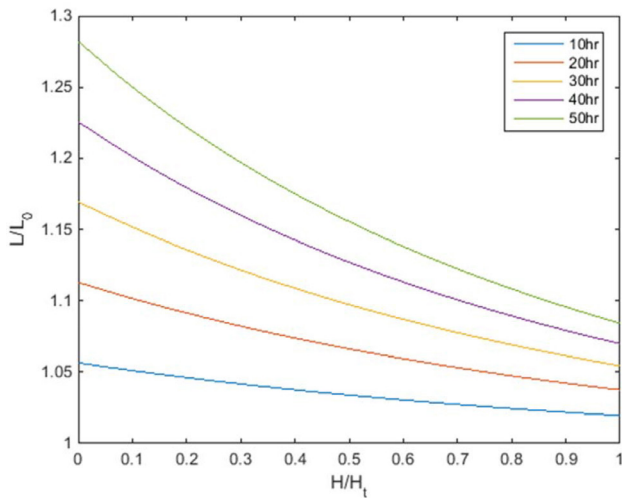Fig. S4. Distribution of relative Ni^{2+} concentration for different feed ratios vs. bed height.
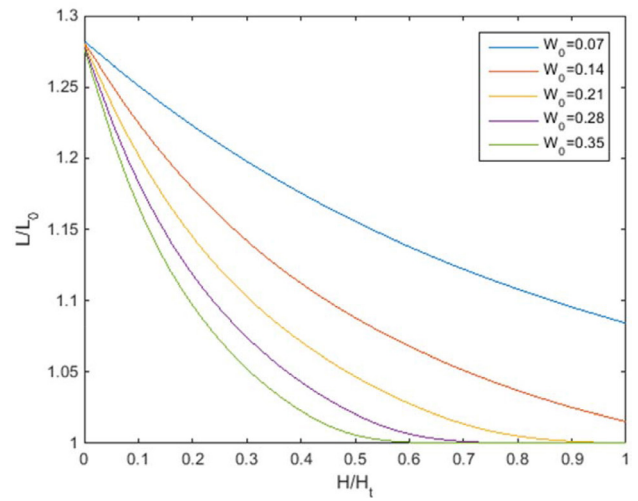
Fig. S5. Relative CaF$_2$ seed diameter at different positions.

Fig. S8. Distribution of CaF$_2$ seed diameter for different amount of seed pellets.
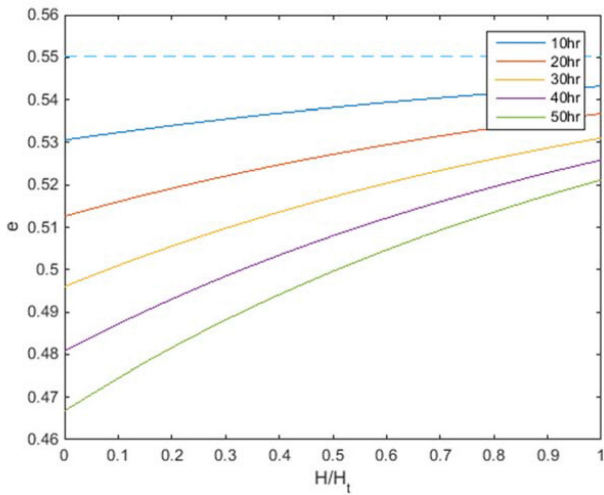
Fig. S6. Bed voidage of CaF$_2$ system at different positions.
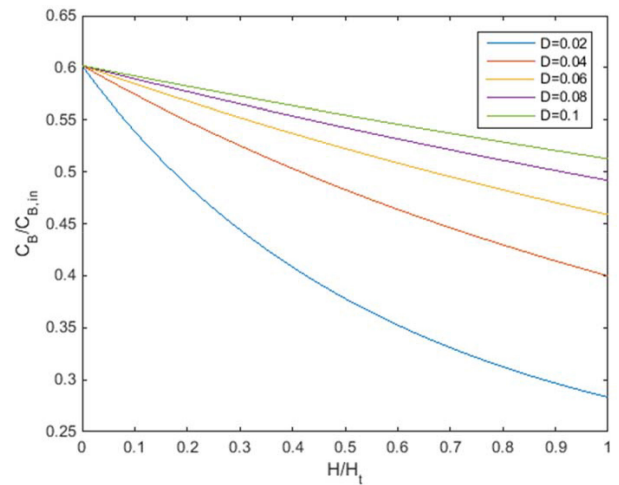
Fig. S9. Concentration profile of F$^-$ for different bed diameters.
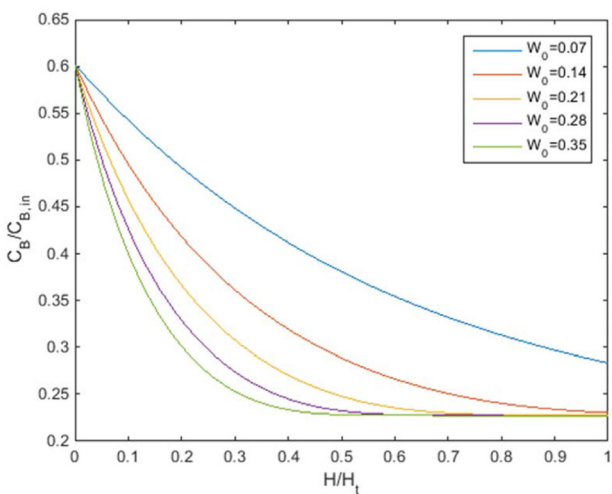
Fig. S7. Concentration profile of F$^-$ for different amount of seed pellets.
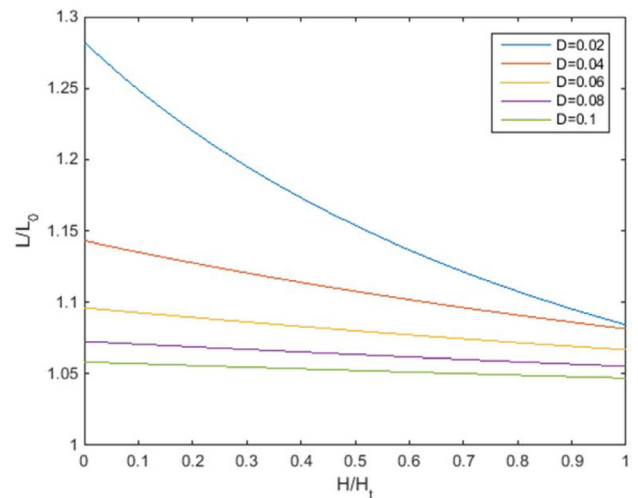
Fig. S10. Distribution of relative CaF$_2$ seed size for different bed diameters.
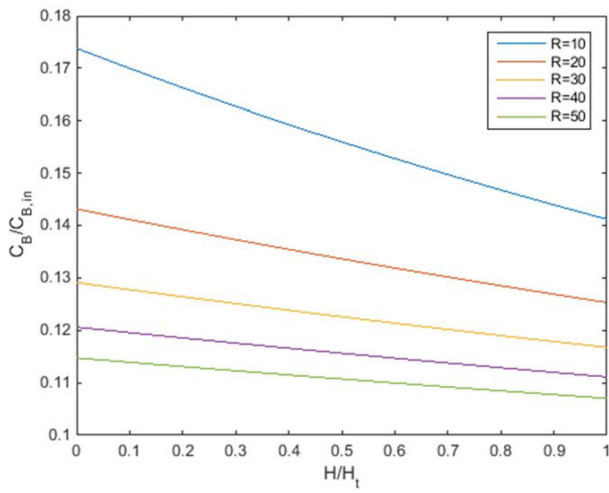
Fig. S11. Concentration profile of F⁻ for different recycle ratios.

Fig. S12. Distribution of relative CaF_2 seed size for different recycle ratios.

Fig. S13. Concentration profile of F⁻ for different feed ratios vs. bed height.
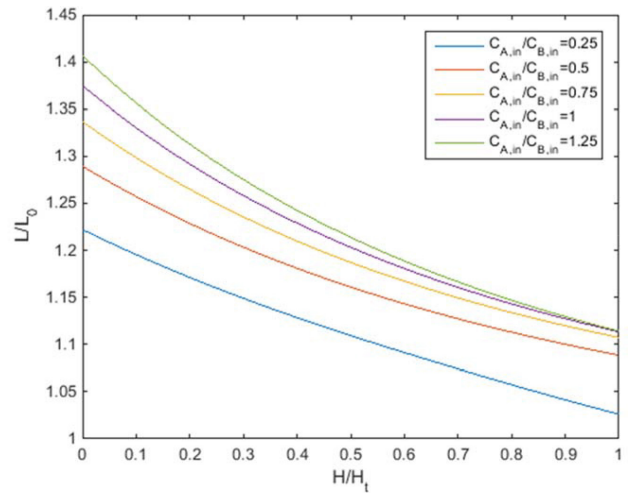
Fig. S14. Distribution of relative CaF_2 seed size for different feed ratios vs. bed height.
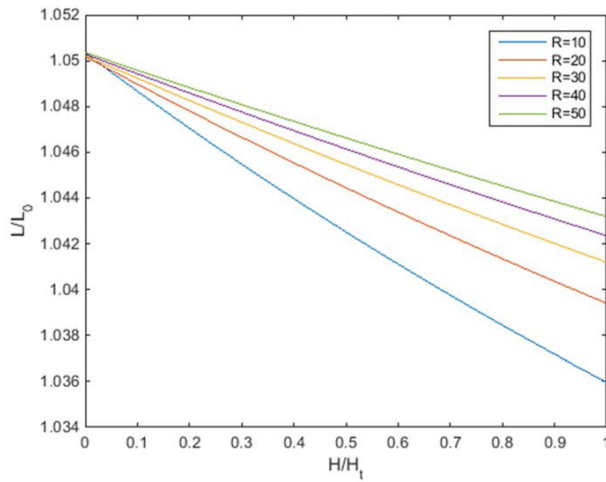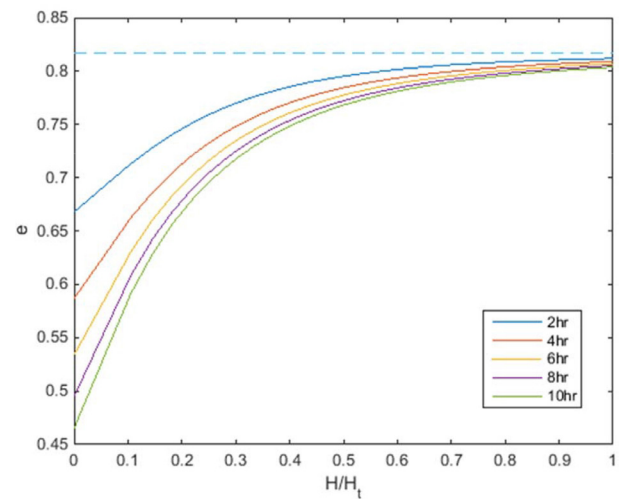
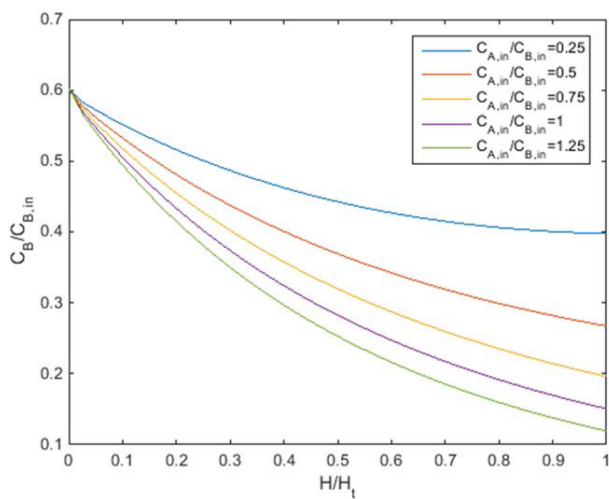Fig. S15. Bed voidage at different positions for struvite system.
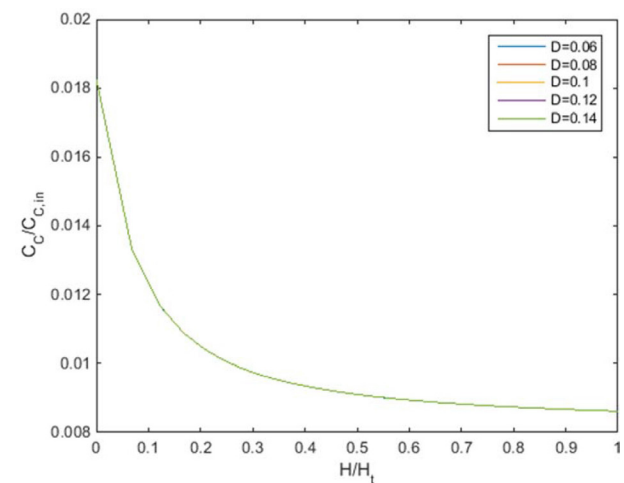
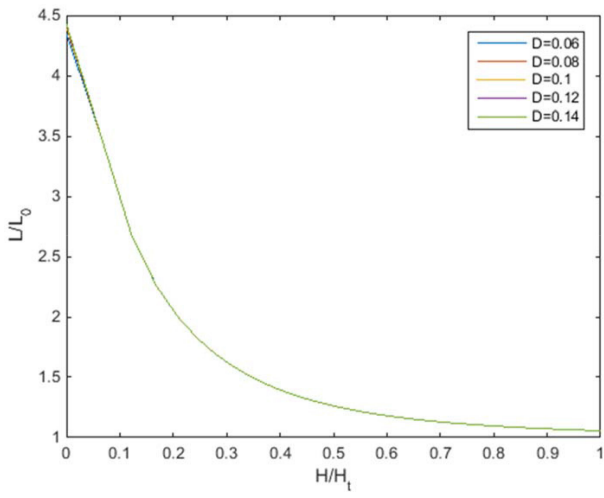Fig. S16. Concentration profile of phosphate for different bed diameters.

Fig. S17. Distribution of relative struvite seed size for different bed diameters.
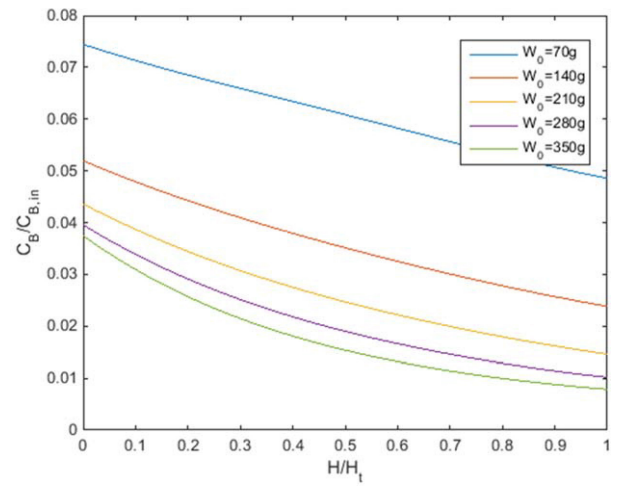
Fig. S18. Concentration profile of F⁻ for different amount of seed pellets.